











## RESEARCH ARTICLE

10.1029/2022JD037694

# Dispersion and Aging of Volcanic Aerosols After the La Soufrière Eruption in April 2021

J. Bruckert<sup>1,5</sup> , L. Hirsch<sup>2</sup>, Á. Horváth<sup>3</sup> , R. A. Kahn<sup>4</sup> , T. Kölling<sup>2</sup>, L. O. Muser<sup>1,5</sup> ,  
C. Timmreck<sup>2</sup> , H. Vogel<sup>1,5</sup> , S. Wallis<sup>6</sup> , and G. A. Hoshyaripour<sup>1,5</sup> 

<sup>1</sup>Institute of Meteorology and Climate Research, Karlsruhe Institute of Technology (KIT), Karlsruhe, Germany, <sup>2</sup>Max-Planck-Institut für Meteorologie, Hamburg, Germany, <sup>3</sup>Meteorological Institute, Universität Hamburg, Hamburg, Germany, <sup>4</sup>Earth Science Division, NASA Goddard Space Flight Center, Greenbelt, MD, USA, <sup>5</sup>Now at Alfred Wegener Institute of Polar and Marine Research (AWI), Bremerhaven, Germany, <sup>6</sup>Institute of Physics, University of Greifswald, Greifswald, Germany

### Key Points:

- Resolving individual eruption phases is essential for modeling the 2021 La Soufrière eruption
- Combination of modeling and satellite data confirm, for the first time, the aging of volcanic ash
- Ash aging and sulfate production rates depend on distance from the source and altitude

### Supporting Information:

Supporting Information may be found in the online version of this article.

### Correspondence to:

J. Bruckert,  
[julia.bruckert@kit.edu](mailto:julia.bruckert@kit.edu)

### Citation:

Bruckert, J., Hirsch, L., Horváth, Á., Kahn, R. A., Kölling, T., Muser, L. O., et al. (2023). Dispersion and aging of volcanic aerosols after the La Soufrière eruption in April 2021. *Journal of Geophysical Research: Atmospheres*, 128, e2022JD037694. <https://doi.org/10.1029/2022JD037694>

Received 19 AUG 2022

Accepted 23 FEB 2023

### Author Contributions:

**Conceptualization:** J. Bruckert, H. Vogel, G. A. Hoshyaripour  
**Funding acquisition:** G. A. Hoshyaripour  
**Investigation:** J. Bruckert  
**Methodology:** J. Bruckert, Á. Horváth, R. A. Kahn, L. O. Muser, C. Timmreck, H. Vogel, G. A. Hoshyaripour  
**Software:** J. Bruckert, L. Hirsch, Á. Horváth, R. A. Kahn, T. Kölling, L. O. Muser, H. Vogel, S. Wallis, G. A. Hoshyaripour  
**Visualization:** J. Bruckert  
**Writing – original draft:** J. Bruckert, G. A. Hoshyaripour

**Abstract** Volcanic aerosols change the atmospheric composition and thereby affect weather and climate. Aerosol dynamic processes such as nucleation, condensation, and coagulation modify the shape, size, and mass of aerosol particles, which influence their atmospheric lifetime and radiative properties. Nevertheless, most models omit these processes for ash particles. In this work, we explore the ash aerosol aging and sulfate production during the first 4 days following the 2021 La Soufrière (St. Vincent) eruption with the ICON-ART model (ICOsahedral Nonhydrostatic model with Aerosol and Reactive Trace gases). Online coupling of ICON-ART with a one-dimensional volcanic plume model calculates volcanic emission, which makes it possible to resolve the different eruption phases of the noncontinuous La Soufrière eruption. We compared our simulated aerosol distribution and composition with observations from the Cloud-Aerosol Lidar with Orthogonal Polarization (CALIOP) instrument, the Multiangle Imaging SpectroRadiometer (MISR) Research Aerosol (RA) Algorithm, and the Barbados Cloud Observatory (BCO). We show that online coupling is essential to adequately model the emissions and plume development close to the volcano. The modeled aerosol aging is in very good agreement with observations from MISR near the emission source and with CALIOP at larger distances. Furthermore, particle aging occurs faster in the troposphere than in the stratosphere due to the availability of water vapor and OH, but a layer of coated ash appears at the plume top due to faster oxidation of SO<sub>2</sub> and lofting by aerosol-radiation interaction. This paper gives the first direct comparison of aerosol aging in volcanic eruption plumes between simulations and observations.

**Plain Language Summary** Large volcanic eruptions can influence weather and climate, and endanger aviation and public health. To constrain these effects and risks, it is critical to reliably predict the volcanic plume dispersion. However, the atmospheric lifetime of the ash released during an eruption is influenced by many factors, such as emission height, meteorology, and aerosol dynamical processes. Aerosol dynamical processes lead to growth and aging of volcanic plume particles. They include the formation of new particles from precursor gases, condensation on existing particles, and coagulation of particles. This paper investigates the formation of aged ash particles in model simulations and observations following the 2021 La Soufrière eruption. We consider ash aging both close to the volcano and during further transport. We found that ash aging takes place already close to the volcano and the fraction of aged particles increases with distance from the source. During further transport, a layer of aged ash particles forms at the plume top due to interaction of these particles with radiation and subsequent warming of the plume.

## 1. Introduction

Large explosive volcanic eruptions can influence weather and climate (e.g., Robock, 2000; Timmreck, 2012; von Savigny et al., 2020). The erupted volcanic material, consisting mainly of ash, water vapor, SO<sub>2</sub>, and other gases, are dispersed in the atmosphere and form secondary volcanic aerosols (e.g., sulfate) during the development of the plume. On long-term climatic time scales, sulfate aerosols modify the radiation by scattering sunlight and, thus, cool the Earth's surface (Robock, 2000; Timmreck, 2012). On weather time scales, volcanic ash can cause circulation changes by radiative heating (Niemeier et al., 2009, 2021). Furthermore, volcanic aerosols can influence the formation of clouds (e.g., Malavelle et al., 2017). The physicochemical properties and atmospheric lifetime of these aerosols modulate their interactions with clouds and radiation. For example, aged ash (coated with sulfate) differs from fresh ash (noncoated) not only in the optical properties (Muser et al., 2020) but also by

© 2023. The Authors.

This is an open access article under the terms of the [Creative Commons Attribution-NonCommercial-NoDerivs License](https://creativecommons.org/licenses/by-nc-nd/4.0/), which permits use and distribution in any medium, provided the original work is properly cited, the use is non-commercial and no modifications or adaptations are made.

**Writing – review & editing:** L. Hirsch, Á. Horváth, R. A. Kahn, T. Kölling, L. O. Muser, C. Timmreck, H. Vogel, S. Wallis

affecting the ice and cloud nucleation (Maters et al., 2020; Umo et al., 2021). To improve our understanding of the impact volcanic eruptions can have on local and global weather, it is essential to constrain the processes that affect the properties and lifetime of volcanic aerosols (e.g., von Savigny et al., 2020).

Aerosols are removed from the atmosphere by wet and dry deposition. The sedimentation of particles depends on their shape, size, and density (Seinfeld & Pandis, 2006). Further aerosol dynamic processes include nucleation and coagulation of aerosol particles, as well as condensation, evaporation, and sublimation of gases on or from aerosols. These processes generate new particles and modify the size and composition of existing particles (particle aging) and, thus, their optical properties and lifetime in the atmosphere (Eriksson et al., 2017; Riemer et al., 2003; Seinfeld & Pandis, 2006). Kahn and Limbacher (2012), Scollo et al. (2012), and Flower and Kahn (2020) investigated particle aging by applying the Multiangle Imaging SpectroRadiometer (MISR) Research Aerosol (RA) algorithm to the plumes of the 2010 Eyjafjallajökull eruption, Etna plumes between the years 2000 and 2008, and three Iceland volcanoes (Eyjafjallajökull 2010; Grímsvötn 2011; and Holuhraun 2014–2015), respectively. Scollo et al. (2012) found that particle type parameters from MISR retrievals, such as the fraction of nonspherical particles and fine mode particles, well reflect the style of explosive activity, i.e., distinguish between ash-dominated and sulfate-dominated or water vapor-dominated plumes. Kahn and Limbacher (2012) further demonstrated that MISR RA is suitable to investigate plume structures and plume particle evolution. Flower and Kahn (2020) used downwind changes in retrieved effective particle size, shape, and light-absorption to infer processes such as size-selective and size-independent gravitational settling, new particle formation, and particle oxidation or hydration.

Several modeling studies have investigated the impact of aerosol dynamics on the formation, properties, and lifetime of volcanic sulfate particles (e.g., Timmreck, 2012). Nevertheless, only a few studies have considered volcanic ash in their model. Niemeier et al. (2009, 2021) studied the effect of aerosol-radiation interaction on the ash and SO<sub>2</sub> dispersion assuming externally mixed aerosols. The results of Niemeier et al. (2009) showed that additional heating and cooling caused by the radiative effect of fine ash particles modifies the evolution of the volcanic cloud. Niemeier et al. (2021) demonstrated that the volcanic emission of very fine ash in the Northern Hemisphere changes the wind patterns in the stratosphere by radiation interaction, influencing the burden and lifetime of sulfate, and altering the radiative forcing. Muser et al. (2020) used the ICON-ART (ICOsahedral Nonhydrostatic model with Aerosol and Reactive Trace gases) model in which the volcanic aerosols (ash and sulfate) were internally mixed for the first time. Their results revealed that aerosol dynamics led to faster removal of volcanic ash from the atmosphere following the Raikoke eruption in June 2019. However, they showed that aerosol-radiation interaction can also lift the volcanic plume top even above the maximum height of emissions by absorbing shortwave (SW) and longwave (LW) radiation, which is in agreement with observations (Chouza et al., 2020). Bruckert et al. (2022) used the same modeling system and additionally found a lofting of the SO<sub>2</sub> as a consequence of the upper plume heating due to absorption of radiation by ash particles. Stenchikov et al. (2021) studied a Pinatubo-size eruption in the equatorial belt by including the radiative effects of SO<sub>2</sub>, ash, sulfate, water vapor, and hydrometeors. Their simulations showed that the volcanic cloud rises by 1 km/day during the first week, primarily due to the ash-induced heating and lofting. The results of Abdelkader et al. (2023) revealed a doubling of the radiative effect in the SW and LW when considering ash aging in climate simulations of Pinatubo-size eruptions. Zhu et al. (2020) showed that the ash particles controlled the chemistry and optical properties of volcanic clouds in the first days to weeks after the Mt. Kelud eruption in 2014. They concluded that persisting volcanic ash particles affected the stratospheric SO<sub>2</sub> lifetime and aerosol optical properties. Despite significant advancements made by these studies, the near-source evolution of volcanic aerosols and their impact on the early stage development of the volcanic clouds are not well understood (Marshall et al., 2022).

In this work, we investigate the evolution of the volcanic plume during the first 4 days after the beginning of the eruption and study the distribution of aged ash particles following the 2021 La Soufrière eruption. The La Soufrière volcano is located on the Caribbean Island of Saint Vincent (13.33°N, 61.18°E). The latest major eruption started on 09 April 2021 and lasted several days. Babu et al. (2022) investigated the long-range transport of the La Soufrière plume using Ozone Monitoring Instrument (OMI) observations. They found that the volcanic plume reached the western North Pacific region about 10 days after the eruption. Modeling the 2021 La Soufrière eruption is challenging, as it was characterized by not one continuous eruption but by a large number of individual pulses (“eruption phases” in the following). Therefore, we use the online approach as in Bruckert et al. (2022), in which ICON-ART is coupled to the one-dimensional volcanic plume rise model FPlume to derive the eruption source parameters (ESPs) for every individual eruption phase. We aim at addressing the following

research questions: (a) What controls the near-source distribution of ash particles? (b) Which processes drive particle aging near the volcano and during the further transport? Here, we directly compare simulated ash aging and observations for the first time; previous studies have investigated the implications of aerosol aging for particle removal and optical properties (e.g., Muser et al., 2020).

This paper is structured as follows: the model system and the observational data are described in Section 2. In Section 3, we first validate our simulated emissions (Section 3.1) and investigate the volcanic plume dispersion (Section 3.2). Then, we focus on the proximal aging of aerosols in the model and in observations (Section 3.3). Subsequently, the far-field aging of aerosols and its dependence on altitude are analyzed (Section 3.4). Finally, we discuss and conclude our findings in Section 4.

## 2. Model and Data Description

### 2.1. ICON-ART

To study the dispersion and aerosol dynamics following the La Soufrière eruption in April 2021, we used the ICON-ART modeling system. ICON solves the nonhydrostatic and compressible Navier-Stokes equations on an icosahedral-triangular grid (Zängl et al., 2015) and allows seamless prediction of various processes from global down to local scales (Giorgetta et al., 2018; Heinze et al., 2017).

ART is a submodule of ICON that enables the simulation of the emission, transport, physicochemical transformation, and removal of trace gases and aerosols in the troposphere and stratosphere (Rieger et al., 2015; Schröter et al., 2018; Weimer et al., 2017). The latest developments in ART further allow a comprehensive treatment of aerosol dynamics and the formation of internally mixed aerosols and their interaction with radiation (Muser et al., 2020).

The volcanic aerosols are organized in seven log-normal distributions considering an Aitken (as soluble), an accumulation (as soluble, insoluble, and mixed), a coarse (as insoluble and mixed), and a giant mode (as insoluble). For the Aitken mode, nucleation, condensation, and coagulation are considered, whereas the accumulation mode and coarse modes are affected by condensation and coagulation only. Shifting of particles into another mode occurs either when the 5% mass threshold of soluble coating on insoluble particles is exceeded (shift from insoluble to mixed mode) or the threshold diameter of the soluble mode (sulfate) is exceeded (shift into larger mode) (Muser et al., 2020).

We performed a global ICON-ART simulation with a 13-km horizontal grid spacing and further horizontal grid refinements to 6.6-km and 3.3-km grid spacing around the volcano by using two nests. The innermost nest resolves convection processes, whereas the global domain and the coarser nest use the Tiedtke-Bechtold scheme for parameterized convection (Bechtold et al., 2008; Tiedtke, 1989). Two-way nesting is enabled, which allows an update of the fields in the parent domain by the child domain at every time step. The model uses 90 vertical levels to resolve the atmosphere up to 75 km. The model time steps are 60, 30, and 15 s in the global domain, first, and second nests, respectively. The simulation starts at 12 UTC on 9 April 2021 and the meteorology is initialized by analysis data provided by the German weather service (DWD). The experiment further includes aerosol-radiation interactions, but neglects the interaction of aerosols and clouds. The emissions of SO<sub>2</sub> and ash by the volcanic eruption are described in the next section.

#### 2.1.1. Volcanic Emission Scheme

The La Soufrière eruption started on 09 April at 12.41 UTC (Joseph et al., 2022) and was characterized by 43 individual phases in the first 4 days and 49 phases during the entire eruption period from 09 to 22 April (Horváth et al., 2022). The detected eruption phases lasted between 10 min and 1 hr, and they reached plume heights between 5.7 and 18.3 km above the vent. In ICON-ART, we parameterize volcanic emissions by coupling to the one-dimensional plume rise model FPlume (Folch et al., 2016) as demonstrated in Bruckert et al. (2022) for the 2019 Raikoke eruption. This feature resolves multiple eruption phases and, thus, allows a more realistic representation of volcanic plume dynamics. FPlume solves the equations of the buoyant plume theory (Morton et al., 1956) along the vertical plume axis and considers processes such as ambient air entrainment, plume bending due to wind, particle wet aggregation, energy supply due to water phase changes, and particle fallout and reentrainment of particles (Folch et al., 2016).

As input parameters, FPlume needs estimates of the plume height, the exit temperature, exit velocity, and exit volatile fraction. The plume heights were geometrically derived from GOES-17 (Geostationary Operational

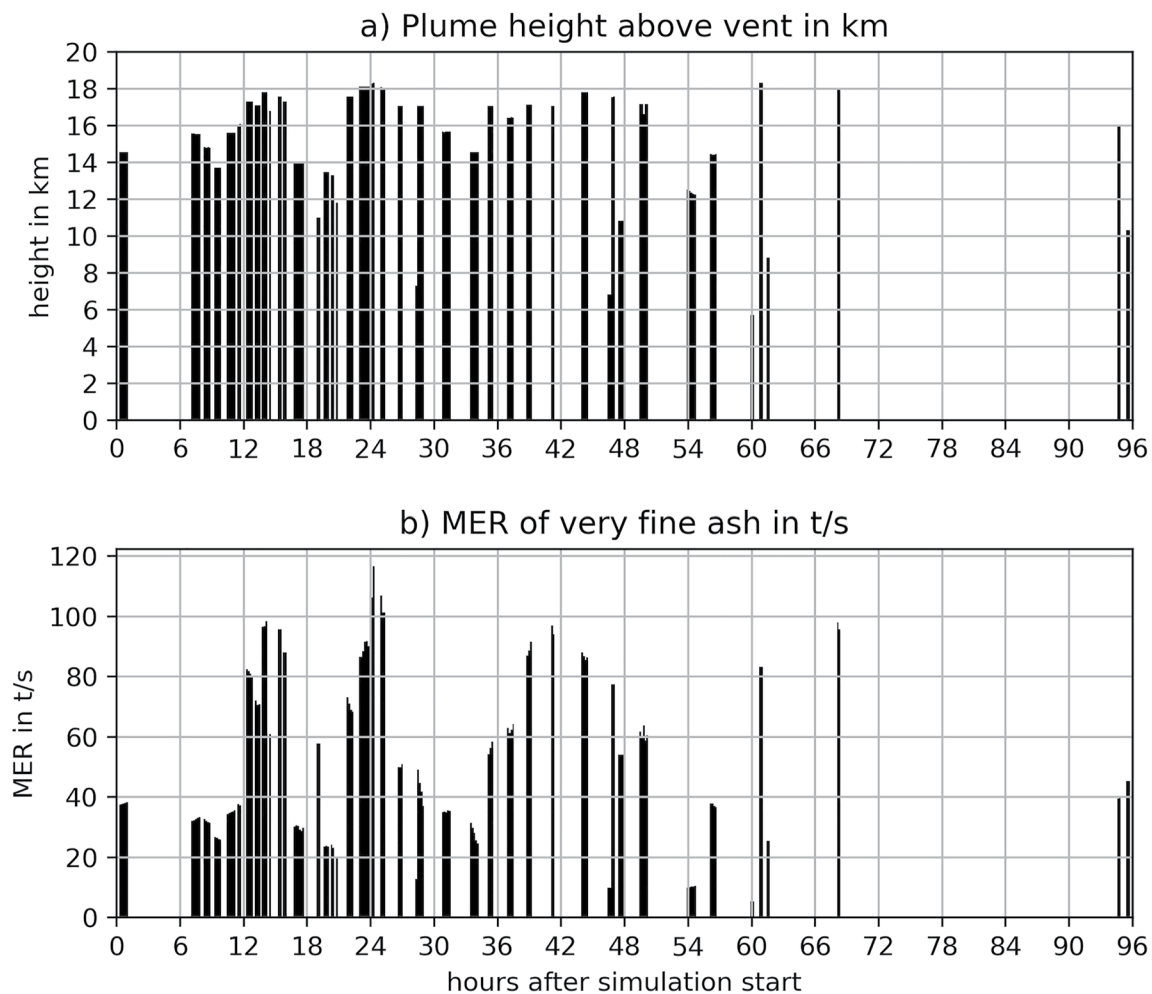


**Figure 1.** Prescribed plume height from satellite estimates (a) and online-calculated emission of very fine ash (b) in the first 96 hr of the 2021 La Soufrière eruption. The emission of very fine ash is derived from the Mass Eruption Rate (MER) modeled with FPlume and a very fine ash parametrization from Gouhier et al. (2019). The bars indicate the timing of the individual eruption phases as well as their length.

Environmental Satellite-17) near-limb imagery at daytime and are temperature-derived from GOES-16 at night-time (Horváth et al., 2022). A detailed description of the geometric side view technique is given in Horváth et al. (2021). The estimates of the exit temperature, exit velocity, and exit volatile fraction were chosen based on Bruckert et al. (2022) for the Raikoke eruption due to a similar composition of the magma: a fixed exit temperature of 1273 K and fixed exit volatile fraction of 3% for all eruption phases; and an exit velocity that is linearly increasing with plume height.

The emission of volcanic compounds in ICON-ART is realized as follows (Bruckert et al., 2022): we calculate the fraction of very fine ash (particles  $<32 \mu\text{m}$  after the definition of Rose and Durant (2009)) relevant for the dispersion in the atmosphere with the total Mass Eruption Rate (MER) derived with FPlume and the input plume height applied to the equation by Gouhier et al. (2019). Figure 1 summarizes the assumed plume heights and the resulting MER of very fine ash for the 43 individual eruption phases. The emission of very fine ash occurred along a Suzuki profile (Marti et al., 2017; Suzuki, 1983), and the mass was evenly distributed as insoluble tracers over the accumulation, coarse, and giant modes. These modes were emitted as log-normal distributions with median mass diameters of 0.8, 2.98, and  $11.35 \mu\text{m}$ , respectively, and a standard deviation of 1.4 for each mode.

### 2.1.2. SO<sub>2</sub> Emission Estimates

The SO<sub>2</sub> mass emitted by the La Soufrière eruption was estimated using data from the TROPOspheric Monitoring Instrument (TROPOMI) aboard the ESA/EU Copernicus Sentinel-5 Precursor (S5P) satellite from 09 to 13

April 2021. The TROPOMI SO<sub>2</sub> total vertical column product used in this study assumes an SO<sub>2</sub> profile with a 1-km thick box filled with SO<sub>2</sub> and centered at 15 km altitude, in order to represent an explosive volcanic eruption (Theys et al., 2017). A grid was defined with a resolution of 0.1° in both latitude and longitude that spans the region between 35°N–30°S and 100°W–30°E. Only SO<sub>2</sub> total vertical columns with values <1,000 mol m<sup>-2</sup> and with a solar zenith angle <70° were used (Theys et al., 2021). All vertical columns were multiplied by the SO<sub>2</sub> molar mass to receive an SO<sub>2</sub> mass loading in units of g m<sup>-2</sup> before a threshold of 0.05 g m<sup>-2</sup> was applied to distinguish the volcanic SO<sub>2</sub> signal from the background. The data passing these criteria were averaged for each grid segment and used to determine the SO<sub>2</sub> mass in units of grams for each segment. As some of the orbits overlap, we always bundled 14 consecutive orbits to a batch that covers ~24 hr and averaged each grid segment of the batch. Finally, the SO<sub>2</sub> mass in all grid segments of a batch were summed up to receive the total SO<sub>2</sub> mass per batch. The highest SO<sub>2</sub> mass per batch was observed on 11 April 2021 and is taken as the best estimate for the total SO<sub>2</sub> mass emitted by the eruption. The resulting amount of SO<sub>2</sub> was 0.4 Tg.

We distributed the total SO<sub>2</sub> amount over the eruption phases by considering the plume height and phase length. The emission occurred along the same profile as for the very fine ash emission. Although this is an idealized assumption, we used this approach because details on the temporal SO<sub>2</sub> emissions during the same eruption phases as derived from GOES-17 are missing. Volcanic emissions of SO<sub>2</sub> and ash can also occur in separate phases (e.g., Thomas & Prata, 2011) or are separated by gravitation in the early stage of the volcanic plume (Prata et al., 2017; Schneider et al., 1999). Taylor et al. (2022) investigated the flux and burden of SO<sub>2</sub> from the La Soufrière 2021 eruption with Infrared Atmospheric Sounding Interferometer (IASI) in more detail. They found that the emission flux of SO<sub>2</sub> was larger on 09 April, which resulted in an SO<sub>2</sub> burden around 0.3 Tg on 11 April, which slightly decreased on the following day. A peak in the SO<sub>2</sub> burden of 0.31 ± 0.09 Tg was reached on 13 April. The authors stated that this amount might be underestimated due to the effects of volcanic ash and the presence of SO<sub>2</sub> below the detection threshold of the instrument. Thus, our value of 0.4 Tg for the SO<sub>2</sub> burden lies at the upper range of the uncertainty of the IASI measurements by Taylor et al. (2022), although our setup does not represent the varying emission flux detected by measurements.

## 2.2. Observational Data

### 2.2.1. Barbados Cloud Observatory

We compared our simulated data to vertical radar data from the Barbados Cloud Observatory (BCO, MPI-M, 2021, downloaded from <https://observations.mpimet.mpg.de/repository/entry/show?entryid=656dc652-e02f-43c9-9378-7307a5143377>). The BCO is located on the east coast of the island of Barbados (13.16°N and 59.43°W) at Deebles Point. The BCO has been operating since 01 April 2010 to advance the understanding of clouds, circulation, and climate sensitivity at the edge of the intertropical convergence zone (Stevens et al., 2016). The La Soufrière volcano is ~150 km west of Barbados. Usually, north-eastern trade winds are prevailing in this region (Stevens et al., 2016). However, at the time of the eruption, Barbados was located at the downwind site of the volcano, which enables the model validation near the volcano.

The BCO is equipped with standard meteorological instruments for temperature, humidity, pressure, wind, rain rate, and solar irradiance measurements, but several remote sensing instruments to study the vertical distribution of overpassing clouds are also installed. In this study, we compared our modeled volcanic compounds to equivalent radar reflectivity data from the Ka-Band (35.5 GHz) cloud radar at BCO to validate the emissions. The temporal resolution of the radar data is 10 s and the vertical resolution is 32 m. The radar measures at range from 150 m up to 18.9 km (Ka-Band Cloud Radar, 2022). Klingebiel et al. (2019) used the BCO Ka-Band radar together with other remote sensing instruments to investigate the sea salt aerosol distribution. As they were able to detect sea salt particles larger than 500 nm, we argue that the Ka-Band radar is able to detect fine mode ash. Thus, we do not need to exclude ICON-ART modes, when we compared the simulation with the BCO radar reflectivities.

### 2.2.2. MISR Interactive eXplorer (MINX) and MISR Research Algorithm (RA)

Plume height and aerosol property data derived from MISR onboard the Terra satellite are compared to ICON-ART simulations on 10 April 2021 at 14:36 UTC, at the Terra overpass time. MISR is a passive sensor measuring upwelling SW radiation in four spectral bands in the visible and near-infrared (446, 558, 672, and 866 nm). MISR provides near-simultaneous coverage at multiple viewing angles, which makes it possible to derive the elevation of lofted features such as volcanic plumes from the parallax between the views. Therefore, the MISR Interactive eXplorer (MINX) software was developed. It is a stand-alone software package used to map volcanic, dust, and



wildfire smoke plume elevations from MISR hyperstereo data (Nelson et al., 2008, 2013). The resulting MINX elevations give a distribution of heights or vertical extent of the plume, keying on the layer of maximum spatial contrast, rather than a value for the absolute plume top height. MISR plume heights are retrieved at the nominal horizontal resolution of 1.1 km. The vertical uncertainty is in the range of 250–500 m (Nelson et al., 2013). In this study, we compare the spatial coverage of the individual eruption phases and their top heights relative to each other in MISR data and simulated ICON-ART data.

The MISR RA algorithm derives constraints on aerosol amount, particle size, shape, and light-absorption properties from the angular-spectral distribution of the scattered light (Kahn & Limbacher, 2012; Limbacher & Kahn, 2014). Thereby modeled radiances are compared with actual radiances measured by the MISR instrument. From this retrieval algorithm, we used the derived total aerosol optical depth (AOD), nonspherical fraction, and single scattering albedo (SSA) to investigate gradients in the horizontal distribution of the particle amount, particle aging, scattering properties, and to infer particle aging processes, within the emitted volcanic plume. The high optical depth of the near-source plume offers favorable conditions for the MISR particle-property retrievals. The values and gradients of the particle-property retrievals are then compared to the same ICON-ART modeled properties at the same plume height as the MINX height.

### 2.2.3. CALIOP/CALIPSO

The CALIPSO satellite (Cloud-Aerosol Lidar and Infrared Pathfinder Satellite Observation) is a joint mission between NASA and the French space agency CNES and was launched on 28 April 2016. The CALIOP (Cloud-Aerosol Lidar with Orthogonal Polarization) instrument onboard CALIPSO provides high-resolution vertical profiles of aerosols and clouds. The measurements are based on the backscattered signal at two wavelengths (532 and 1,064 nm). Two channels receive orthogonally polarized components of the 532 nm backscattered signal, whereas the 1,064 nm backscatter intensity is only received at one channel (Winker et al., 2009).

We here used the total attenuated backscatter at 532 nm from CALIOP L1 data version 4.11 (downloaded from [https://asdc.larc.nasa.gov/data/CALIPSO/LID\\_\\_L1-Standard-V4-11/2021/04/](https://asdc.larc.nasa.gov/data/CALIPSO/LID__L1-Standard-V4-11/2021/04/)) and compared this to our simulated signals. Furthermore, we used the CALIOP depolarization ratio at 532 nm from the ratio of the perpendicular and parallel attenuated backscatter at 532 nm. This allows an estimation of whether the plume is dominated by spherical (i.e., coated particles or droplets) or nonspherical compounds (i.e., uncoated aerosol particles) (Winker et al., 2009). In total, 13 CALIPSO overpasses traversed the plume within the first 4 days of the eruption. In order to compare the CALIPSO total attenuated backscatter signal with ICON-ART modeled data, we applied the forward operator described by Hoshyaripour et al. (2019). According to Hoshyaripour et al. (2019), the total attenuated backscatter for the 532-nm wavelength is calculated with the following equation:

$$\epsilon(z) = \beta_b(z) \exp\left(-2 \sum_{i=1}^z \beta_e(z_i) \Delta z_i\right)$$

with  $z$  height in m,  $\beta_b$  the volume backscattering coefficient, and  $\beta_e$  the volume extinction coefficient in  $\text{m}^{-1}$ .  $\beta_b$  and  $\beta_e$  are determined by summing over all modes  $l$

$$\beta_e = \sum_l k_{e,l} \rho_a m_l$$

$$\beta_b = \sum_l k_{b,l} \rho_a m_l$$

with  $\rho_a$  the density of air in  $\text{kg m}^{-3}$  and  $m_l$  mass mixing ratio of mode  $l$  in  $\text{kg kg}^{-1}$ .  $k_{e,l}$  and  $k_{b,l}$  are the mass specific extinction coefficient and mass specific backscattering coefficient for the individual modes in  $\text{m}^2 \text{kg}^{-1}$ . For simplification, the values for  $k_{e,l}$  and  $k_{b,l}$  are fixed within each mode and depend only on an average value for the radius and composition of mode  $l$ .

## 3. Results

### 3.1. Vertical Distribution of Ash Near the Volcanic Source

In this section, we first validate the modeled volcanic emission with observed radar reflectivity data from BCO ~150 km east of the La Soufrière volcano. Figure 2 shows in the top row the temporal development of equivalent radar reflectivity from BCO for all targets in dBZ (decibel relative to the equivalent reflectivity factor Z), and the

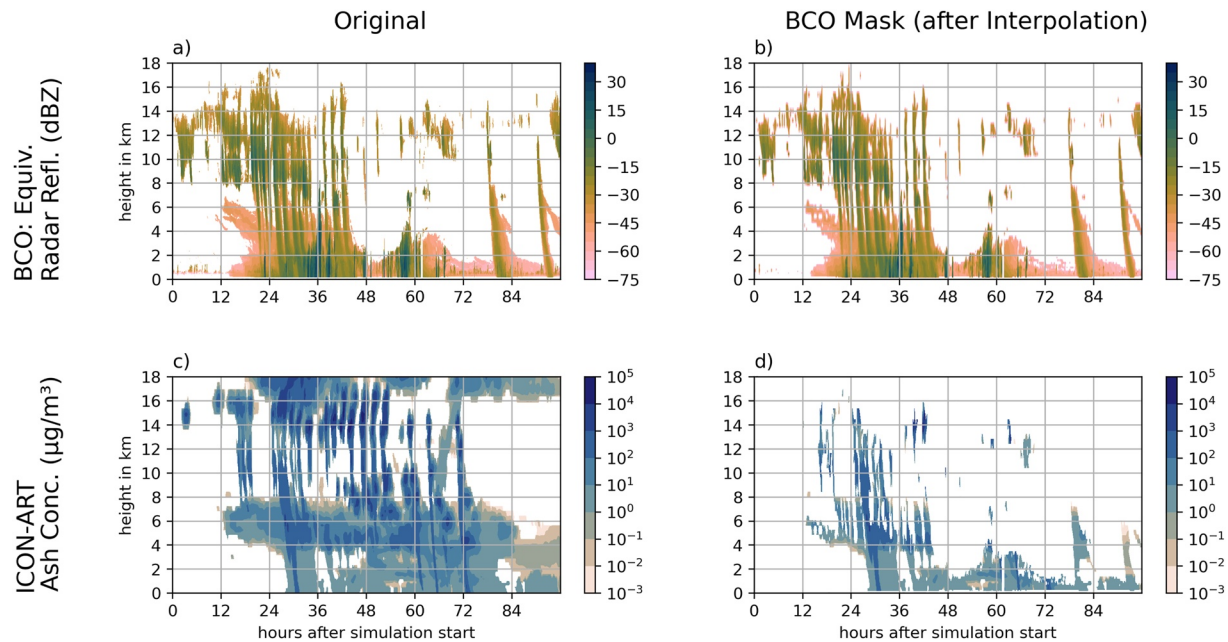


**Figure 2.** Top row: BCO equivalent radar reflectivity for all targets in dBZ; bottom row: ICON-ART ash concentration above Barbados in  $\mu\text{g m}^{-3}$ . The left column shows the original data and the right column shows the data after interpolation onto the ICON-ART vertical grid for the BCO data (top right) and the ICON-ART ash concentration with the interpolated BCO mask (bottom right).

bottom row shows the temporal development of total ash concentrations in  $\mu\text{g m}^{-3}$  for the ICON-ART experiment at the same location, respectively. The left column (a and c) shows raw data, whereas the right column (b and d) depicts the radar data gridded onto the ICON-ART vertical grid (Figure 2b) and the simulated data masked according to the points of no detected reflectivity in the BCO radar measurements (Figure 2d).

A noticeable difference between model and observations occurs from 48 to 72 hr after the start of the eruption between 3 and 8 km. The radar shows no reflection, whereas ICON-ART indicates enhanced ash concentrations. The BCO data show increased rain intensity before this period (not shown). This leads to ash removal by wet deposition, which is underestimated in the model due to the lack of precipitation. As the rain does not only occur above the BCO site but also upwind of Barbados, this leads to a stronger removal from the atmosphere and less ash transport toward Barbados from surface to 8 km altitude.

The radar observations indicate several maxima in the reflectivity data up to 18 km most likely originating from reflection by volcanic ash particles from the La Soufrière eruption. Good agreement with the model is especially visible when using the radar reflectivity mask onto the simulated ash concentrations (right column). Although this is only a qualitative analysis, it confirms that considering the individual phases of the La Soufrière eruption is important to correctly represent the development of the volcanic plume in the near-field of the volcano. The maximum height of detection for the BCO radar is around 19 km, which explains the discrepancy between model and observations at altitude ranges above. Discrepancies at 16–18 km arise from both a lower sensitivity of the radar and strong radar attenuation at lower altitudes. Further reasons for the differences between model and observations are related to both model and measurement uncertainties. The most important model errors are associated with the initialization of the volcanic emissions, and problems in the representation of the dispersion and fallout of aerosol particles. On the observational side, dense ash or other particles in the atmosphere weaken the penetration of the radar signal, which underestimates the reflectivity in higher altitudes (above 5 km).

Both the radar observations and the modeled ash concentrations indicate vertically orientated streaks below the peaks of the eruption phases. These vertical streaks are not related to fall streaks, but rather originate from a vertical wind shear affecting the dispersion of the plume column. The gravitational settling velocity of the emitted particles is on the order of up to  $5 \times 10^{-4} \text{ m s}^{-1}$  for the accumulation mode (around  $0.8 \mu\text{m}$  in diameter) to  $0.04 \text{ m s}^{-1}$  for the giant mode (around  $12 \mu\text{m}$  in diameter), respectively, assuming spherical particles. The distance from the volcano is roughly 150 km and the temporally varying horizontal wind profile above Barbados ranges from 0 to  $25 \text{ m s}^{-1}$  (see in Supporting Information S1). Based on these factors, we can calculate a typical settling height change of the

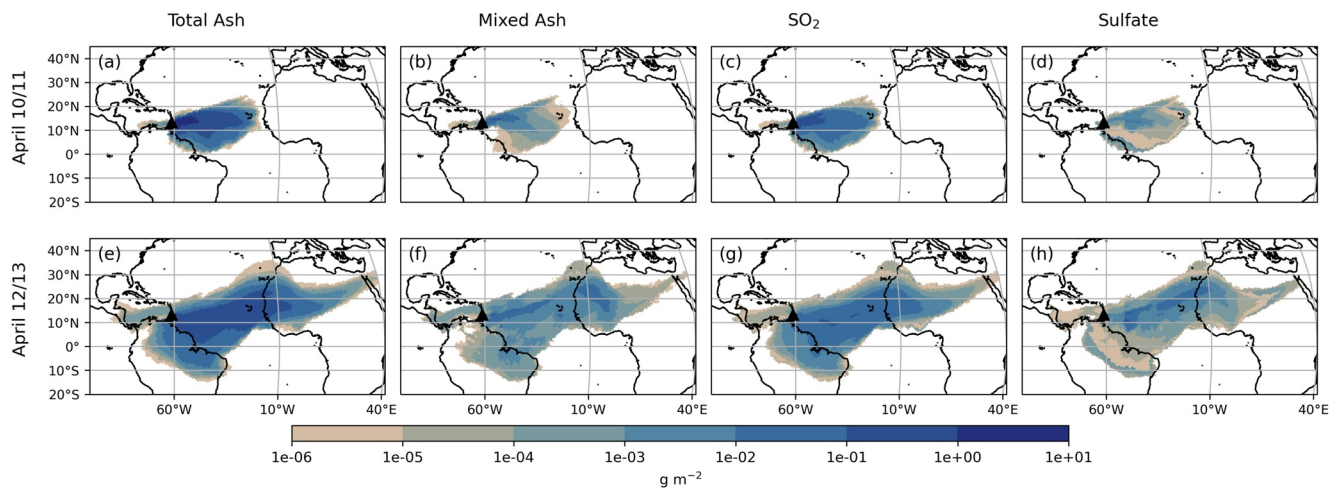


**Figure 3.** Twenty-four-hour averages for (a) total very fine ash, (b) coated ash, (c)  $\text{SO}_2$ , and (d) sulfate column loadings in  $\text{g m}^{-2}$  for 10 April 2021 at 12 UTC till 11 April 2021 at 11 UTC. (e), (f), (g), and (h) same as (a), (b), (c), and (d) but for 12 April 2021 at 12 UTC till 13 April 2021 at 11 UTC. The black triangle indicates the location of the La Soufrière volcano.

particles between the La Soufrière volcano and Barbados. The gravitational settling is on the order of a few meters for the accumulation mode and a few hundred meters for the giant mode during the transport from the volcano to Barbados, respectively. Therefore, the vertical streaks in Figure 2 cannot be related to particle fallout. The vertical distribution split into the different modes further supports the transport of particles at different wind speeds instead of fall streaks, because the vertical streaks are visible for all particle sizes in the model (in Supporting Information S2).

We conclude that the timing of the volcanic emissions in the model are well represented and allow a distinction of the individual eruption phases. This confirms that the near-source distribution of very fine ash is mainly affected by eruption dynamics and the wind shear rather than aerosol dynamic processes. In the following, we focus on the further plume dispersion across the Atlantic Ocean.

### 3.2. Plume Dispersion

In this section, we focus on the volcanic plume dispersion across the Atlantic Ocean. Figure 3 shows 24-hr-averages from 10 April at 12 UTC to 11 April at 11 UTC (a, b, c, d) and from 12 April at 12 UTC to 13 April at 11 UTC (e, f, g, h) for total very fine ash (a, e), coated ash (mixed ash, b, f),  $\text{SO}_2$  (c, g), and sulfate (d, h) column loadings. The simulations show a dispersion of the volcanic plume toward the east across the Atlantic Ocean, which reaches the African coast after  $\sim 2.5$  days. The structure of the total ash,  $\text{SO}_2$ , and sulfate plumes looks similar, indicating transport of all compounds at the same altitude with low vertical separation or a small vertical wind shear in the altitude of the main mass transport.

On both days, the total ash and  $\text{SO}_2$  plumes show maximum column loadings east of the volcano spreading zonally and decreasing column loadings toward the edges of the plume. In contrast, multiple local maxima occur in the coated ash and sulfate plumes. In the case of the sulfate plume, this happens because the sulfate production depends on the availability of OH, which is predominately produced during daytime. Coated ash forms by condensation of water and/or  $\text{H}_2\text{SO}_4$  onto preexisting particles or by coagulation with sulfate particles. Thus, the coated ash formation also depends on the diurnal cycle (Supporting Information S3).

To understand the driving processes, in the next sections, we focus on the formation of coated ash and sulfate in comparison with observations close to the volcano (Section 3.3) and during the further plume dispersion (Section 3.4).

### 3.3. Proximal Aging of the Aerosols

#### 3.3.1. Plume Height Validation

Due to the narrow coverage of the MISR instrument ( $\sim 380$ -km wide swath, Kahn & Limbacher, 2012), which is especially significant at low latitudes due to its polar orbit, the volcanic plume is only observed on 10 April 2021 at 14:36 UTC. Fortunately, MISR happened to capture the approximate peak of the eruption event. We first



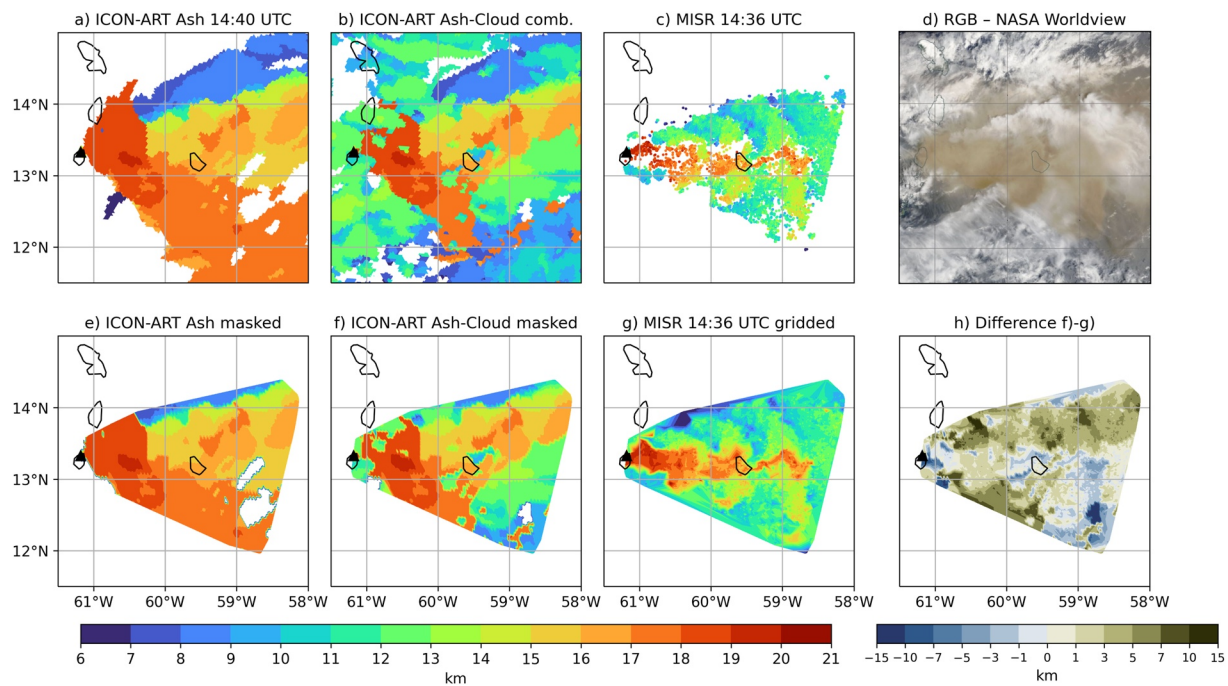


**Figure 4.** (a) ICON-ART ash plume top heights with a detection threshold of AOD > 0.2 at 14:40 UTC on 10 April 2021; (b) ICON-ART combined ash plume top heights and cloud top heights; (c) Multiangle Imaging SpectroRadiometer (MISR) plume top height at 14:36 UTC on 10 April 2021; (d) MODIS true color image at 14:36 UTC on 10 April 2021 from the NASA Worldview webpage (<https://worldview.earthdata.nasa.gov/?t=2021-04-10-T09%3A12%3A58Z>); (e) and (f) same as (a) and (b), but interpolated on a regular latitude-longitude grid and only showing values where MISR data are available; (g) same as (c), but interpolated on a regular latitude-longitude grid; (h) difference between ICON-ART ash-cloud combined height and MISR height (f) and (g).

discuss the difference between the modeled and observed plume height, and then analyze the aerosol properties in ICON-ART and the MISR RA product. We use a threshold of AOD > 0.2, to separate the modeled ash plume from background concentrations. This value is similar to the particle-property retrieval threshold of MISR (Kahn & Gaitley, 2015; Kahn et al., 2001).

Figure 4 shows simulated and observed plume top heights (a–c, e–g), an MODIS (MODerate-resolution Imaging Spectroradiometer) true color from the NASA Worldview webpage (d, <https://worldview.earthdata.nasa.gov/?t=2021-04-10-T09%3A12%3A58Z>), and the difference between simulated and observed heights (f and g in panel h). The first three plots in the top row display the original data (a–c), whereas the data in the bottom row is interpolated onto a regular latitude-longitude grid and only shows values where MISR heights are available (d–f). ICON-ART ash plume top heights are higher than the MISR heights in large parts of the displayed region (Figures 4a and 4c). The MINX stereo algorithm used to derive the MISR heights is sensitive to the contrast features in atmospheric aerosol plumes or clouds and Earth's surface over land and water, which might complicate a separation of meteorological clouds and ash plumes (Nelson et al., 2008). The NASA Worldview RGB image in Figure 4d reveals a thick meteorological cloud north of Barbados. Furthermore, most of the area beneath the brownish ash plume is covered by meteorological clouds. Stereo matchers generally track the lower layer in a two-layered scene when optical depth of the top layer is relatively small (e.g., Mitra et al., 2021). We therefore combined the simulated ash top heights with the cloud top heights from the model. The cloud top heights are obtained from the vertical profiles of liquid water and cloud ice mixing ratios at every point in the region of interest (maximum height where profiles are nonzero). Next, we combined the ash plume top height and the maximum cloud heights such that if the ash column AOD above the cloud is lower than a prescribed threshold, the cloud height is used and otherwise or in the absence of clouds the ash height is used. We achieved the best agreement with the observations when using a modeled AOD threshold of 10.0, where clouds are present (elsewhere the detection threshold of AOD > 0.2 was applied). The result is given in Figures 4b and 4f.

The ash-cloud combined heights from the model agree better with the MISR heights than the raw ash plume top heights. Although the threshold and assumptions used to derive the ash-cloud combined height are iterative, this procedure highlights the role of clouds in obtaining the correct ash plume top height from satellite observations,

especially when comparing with model simulations. We further want to note here that volcanic eruptions often emit large amounts of water vapor. This water vapor can condense and/or freeze, and coat on ash particles. So, the distinction between the ash plume and water or ice clouds in the immediate vicinity of the volcano might be ambiguous.

The MISR data cover a smaller region than we modeled with ICON-ART, which gives the impression that ICON-ART ash and even ash-cloud combined height differ significantly from the MISR observed heights. However, when only viewing the region where MISR data are available, there is a good agreement between ICON-ART ash-cloud combined and MISR heights with respect to the maximum and minimum plume heights (Figures 4f and 4g). Between the volcano and Barbados along 13.1°N, the differences are on the order of  $\pm 5\%$  indicating a good agreement when the ash plume is thick and less cloud is visible (Figure 4d). Further, it is possible to distinguish different eruption phases in the plume height data. However, the eruption phases seem more apparent and more confined along the latitude of the eruption in the MISR observations than in the model. In the northern part of the plume, there is a positive bias in the ICON-ART heights relative to the MISR heights because our model could not reproduce the thick cloud north of Barbados (Figures 4e–4g).

The south-eastern direction of the dominant ash dispersion in ICON-ART at the plume top in Figures 4a, 4b, 4e, and 4f originates from a clockwise rotation of the horizontal winds with height in the model (Supporting Information S4). The observations, in contrast, show a largely zonal dispersion. This is a limitation of the model rather than a MISR retrieval artifacts. The most likely problem here is the vertical resolution in upper cells of the plume (around 20 km altitude), which is on the order of 800 m. In case the prescribed plume height for the emission is between two levels, it is assigned to the upper level. Uncertainty in the determination of the emission height is on the order of  $\pm 500$  m and might additionally lead to an imprecise emission profile and, thus, a wrong direction of transport in the upper layers of the plume. Considering the large uncertainties in the ESPs, the error in the modeled winds is of minor importance here.

### 3.3.2. Aerosol Properties

The previous section revealed similarities but also differences between the top height from MISR MINX and ICON-ART, which are mainly related to the presence of meteorological clouds in the plume region. Therefore, we compare the aerosol properties such as AOD, fraction of spherical particles, and SSA at the level of the MISR cloud top height. The layer thickness (needed for the AOD) was calculated as the difference between the maximum and minimum height (from MISR MINX) in a  $0.6^\circ \times 0.6^\circ$  box around the individual data point. The box size is in the range of the spatial resolution of the MISR MINX (Nelson et al., 2013) and MISR RA (Limbacher & Kahn, 2014). The simulated fraction of spherical particles was calculated as the AOD of spherical particles (sulfate and coated ash) divided by the total AOD for comparison with MISR RA in this section.

Figure 5 shows the spatial maps of particle-property values from the MISR RA and ICON-ART the plume AOD at 550 nm, the fraction of spherical particles, and the SSA at 550 nm. The AOD refers to the amount of particles in the plume column, assessed at midvisible wavelengths. The fraction of spherical particles gives information about the aging of the plume and was derived from the ICON-ART data from the soluble plus the mixed mode AOD divided by the total AOD. The SSA indicates the composition of the plume. We only qualitatively compare the two data sets and concentrate on the spatial gradients in the plume. The absolute values of the retrieved parameters are highly uncertain due to the large amount of meteorological clouds in the region around La Soufrière and the retrieval assumptions.

The AOD values in both MISR RA and ICON-ART indicate a thick plume branch between La Soufrière and a half degree north of Barbados (Figures 5a and 5d). The values in the other parts of the plume are strongly reduced. However, the spatial reduction of the AOD values in ICON-ART is stronger than in the MISR RA. We note that the total AOD has to be treated with caution due to uncertainties in the thickness of the volcanic plume in the model simulation and the meteorological clouds that can affect the MISR retrieval, either with cloud contamination, or by hygroscopic particle growth. In particular, the thick cloud band north of Barbados along the main direction of the plume dispersion, which is in the true color picture (Figure 4d), is missing in the simulations.

The MISR RA and ICON-ART agree very well in terms of fraction of spherical particles and SSA south of Barbados. Especially the observed pattern and inferred evolution of particle aging along the longitudes below 15.3°N are well represented by ICON-ART. With increasing distance from the source, the fraction of spherical particles increases due to the formation of sulfate and/or condensation of  $\text{H}_2\text{SO}_4$  and/or water on ash. The SSA decreases from west to east because the scattering is larger for aged volcanic particles than for fresh ash (Muser et al., 2020).

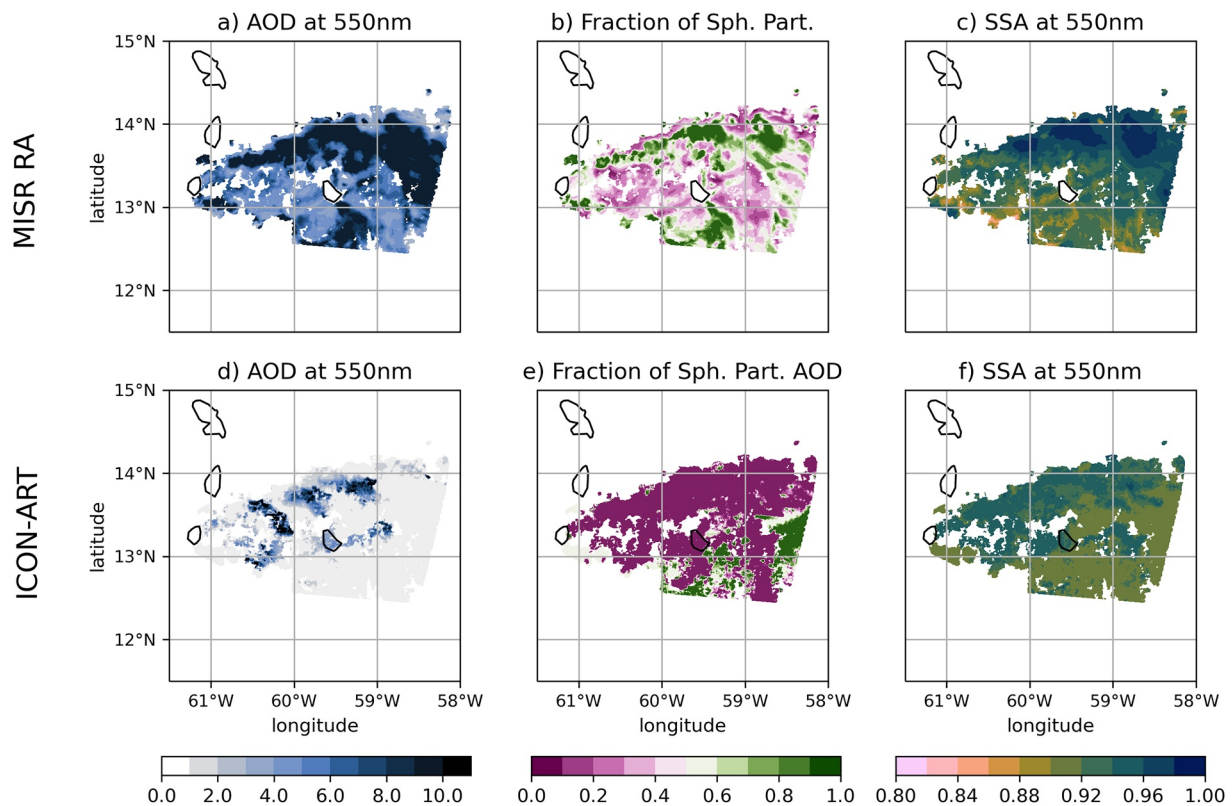


**Figure 5.** (a–c) Multiangle Imaging SpectroRadiometer (MISR) plume aerosol optical depth (AOD) at 550 nm, MISR fraction of spherical particle, and MISR single scattering albedo (SSA) at 550 nm, respectively; (d), (e), and (f) same as (a), (b), and (c) but for ICON-ART at the altitude range of the MISR volcanic plume as detected by MINX. ICON-ART fraction of spherical particles was calculated as the AOD of spherical particles divided by the total AOD.

North of Barbados, the MISR fraction of spherical particles and SSA shows that the plume is dominated by strongly scattering spherical particles, such as sulfate, and/or hydrometeors (Figures 5b and 5c). The true color image in Figure 4d shows a thick band of meteorological clouds north of Barbados. Thus, the large fraction of spherical particles in the north might be a result of a large abundance of hydrometeors. In ICON-ART, the northern part of the plume mainly consists of nonspherical particles which are only slightly more light scattering than south of Barbados. However, ICON-ART is not able to capture the meteorological cloud band north of Barbados. Instead, increased SSA values in the model occur because the ash particles in the northern plume are slightly smaller on average. A reason might be that the modeled plume heights are closer to the observed height in the northern part than in the southern part (Figures 4e and 4g). The ICON-ART aerosol properties in Figures 5d and 5f then refer to a higher plume height relative to the actual maximum plume height, and the plume contains on average smaller particles due to sedimentation of the larger ones.

The MISR RA fraction of spherical particles appears more noisy, especially in the northern part of the plume (Figure 5b). This part is also largely covered by clouds (Figure 4d), which increases the measurement uncertainties. Kahn et al. (2001) report increased confidence in MISR aerosol type retrieval when the component contributes at least about 20% to the total AOD.

The individual eruption phases of the La Soufrière eruption are especially visible in the ICON-ART AOD and manifest as individual arcs of plumes (Figure 5d). In the AOD of the MISR RA, the eruption phases are smoothed out, although they can be distinguished in the MISR MINX plume top heights (Figure 4c). The southern part of the plume in ICON-ART reveals low AOD values (Figure 5d). We therefore argue that the large plume top heights in the southern plume in Figure 4e originate from a thin plume layer rather than indicating a large mass transport in the wrong direction.

With the comparison to the MISR aerosol product, we looked at the horizontal distribution of the plume aging close to the eruption. In the next section, we investigate differences of the aging at larger distances from the volcano.

### 3.4. Distal Aging of the Aerosols

In this section, we first validate the far-distance aging of the La Soufrière aerosol particles by comparing ICON-ART with CALIOP attenuated backscatter and depolarization ratio. Subsequently, we focus on the aging and sulfate production at different altitudes and with increasing distance from the source region.

#### 3.4.1. Validation Along Satellite Track

The CALIPSO satellite passed over the volcanic plume on 13 April 2021 around 5 UTC. Figure 6a shows the modeled ash and sulfate column loading on this day from the ICON-ART experiment in colors together with the CALIPSO ground track. The corresponding total attenuated backscatter signals from the CALIOP instrument and ICON-ART are given in Figures 6b and 6d, respectively. Figure 6c refers to the CALIOP depolarization ratio and Figure 6e is the modeled fraction of spherical particles defined as the mass of spherical particles divided by the total mass. The fraction of spherical particles only shows areas where the ICON-ART total attenuated backscatter is larger than  $2 \times 10^{-4} \text{ km}^{-1} \text{ sr}^{-1}$ , in order to clearly separate the modeled plume from background concentrations. Eighty-nine hours after the eruption start, the ash plume covers most parts of the tropical and subtropical Atlantic Ocean, and North-West Africa (Figure 6a).

Based on the modeled attenuated backscatter signals, the volcanic plume in ICON-ART reaches a top height of 20 km between 15°N and 20°N along the satellite path, which agrees well with the uppermost signal in the CALIOP data at the same location (Figures 6b and 6d). A stratospheric volcanic plume layer exists between 10°S and 15°N in an altitude range from 15 to 20 km in both CALIOP measurements and ICON-ART modeled data. However, the strength of the signal is larger in ICON-ART. Besides larger particle concentration itself, a large source of uncertainty is also the calculation of the attenuated backscatter signal with ICON-ART (see Section 2.2.3).

The stratospheric volcanic plume layer consists of mainly spherical particles because the CALIOP depolarization ratio is between 0.1 and 0.2 (Figure 6c). ICON-ART spherical particle fraction mainly agrees with this finding, at least for the uppermost part of this stratospheric volcanic plume layer (Figure 6e). The upper tropospheric regions of the plume in ICON-ART (between 10 and 15 km), where nonspherical particles are dominant, is lacking in both the CALIOP total attenuated backscatter and CALIOP depolarization ratio.

In the troposphere, ICON-ART total attenuated backscatter signals are enhanced between 10°S and 18°N and 5–10 km, which is only partly visible in the total attenuated backscatter signals of CALIOP (Figures 6b and 6d). However, the CALIOP depolarization ratio reveals spherical particles (depolarization ratio of about 0.1–0.3) close to the locations of increased total attenuated backscatter signals in the troposphere in ICON-ART (Figures 6c and 6d). The ICON-ART spherical particle fraction in Figure 6e shows that the plume is dominated by spherical particles at this location, which agrees well with the features in the CALIOP depolarization ratio (Figure 6c).

The CALIOP attenuated backscatter data shows two distinct signals around 5°S and 5°N between 12-km and 16-km altitude, with a depolarization ratio of about 0.4 (Figures 6b and 6c). The attenuated backscatter in ICON-ART is very low in this area (Figures 6c and 6e). The CALIPSO vertical feature mask reveals that these features arise from ice clouds (not shown) as well as the attenuated backscatter signal north of 25° between 8 and 12 km in Figure 6b. The weakly depolarizing features below 5-km altitude north of 5°N (Figures 6b and 6c), which are not simulated by ICON-ART, are dust and sea salt aerosols according to the CALIPSO aerosol subtypes (not shown).

Besides this time step, the CALIPSO satellite crossed the volcanic plume from the La Soufrière eruption on 12 additional occasions. The agreement between CALIOP measurements and ICON-ART is similar for these dates (in Supporting Information S5–S16).

#### 3.4.2. Temporal Average

Having validated the aging with different types of data sets at fixed locations, we now want to examine whether aerosol aging is height-dependent. Figures 7a and 7b show height-longitude cross-sections averaged over all model output time steps (hourly global output) along the latitudes 11.08°–15.58°N ( $\pm 2.5^\circ$  of the latitude of the volcano) for the spherical modes (mixed + soluble) and mixed mode proportions of the total ash and sulfate mass, which is related to the particle composition and aging. Figures 7c and 7d show the same but for the accumulation and coarse mode proportions of the total ash, i.e., this provides information on particle size. The total ash always refers to the sum of accumulation insoluble and mixed, coarse insoluble and mixed, and the insoluble giant mode.



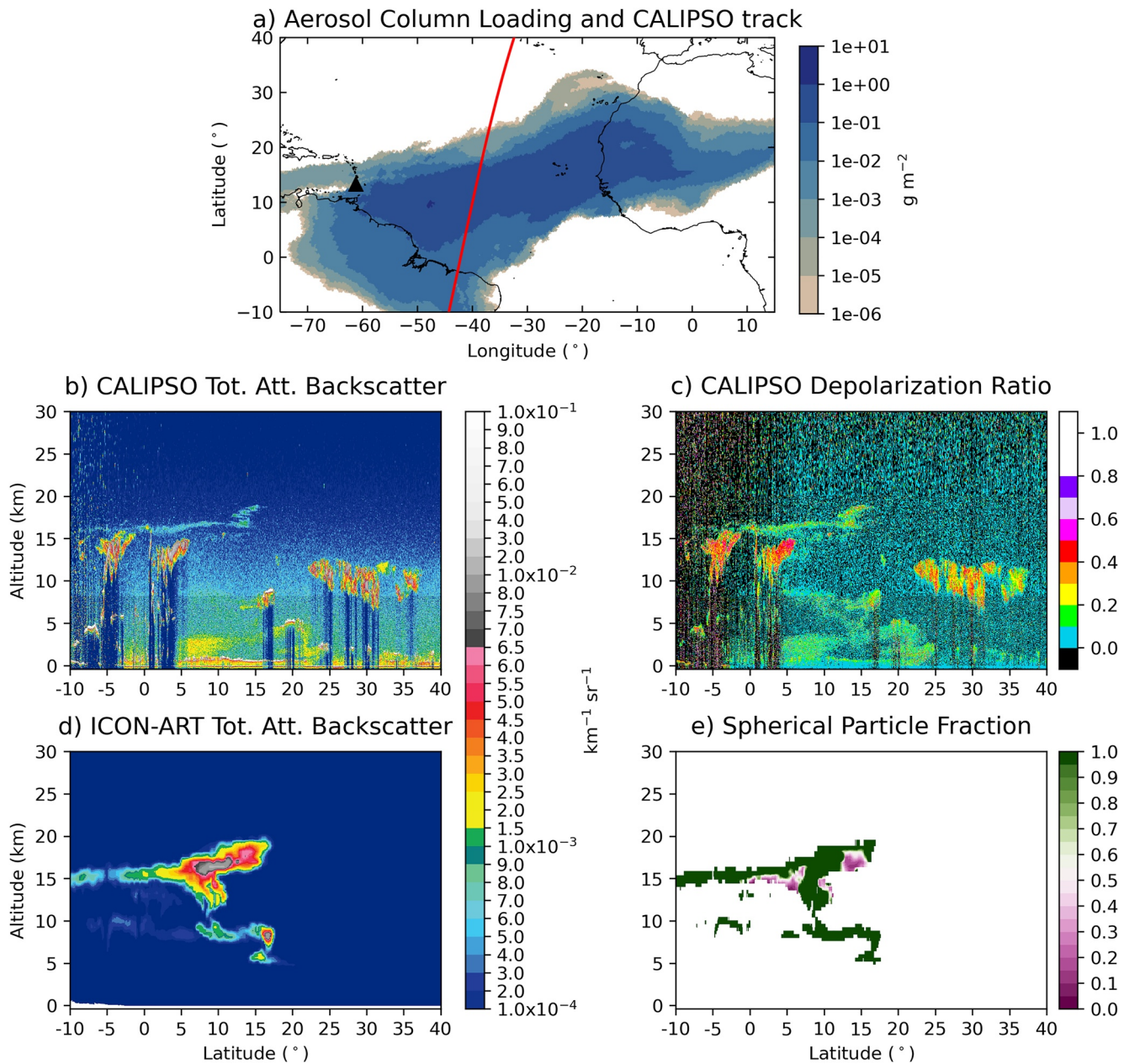


**Figure 6.** (a) Ash and sulfate column loading in  $\text{g m}^{-2}$  from the ICON-ART experiment together with the CALIPSO ground track in red on 13 April 2021 around 5 UTC and the La Soufrière volcano as a black triangle. According, (b) CALIPSO total attenuated backscatter at 532 nm, (c) CALIPSO depolarization ratio at 532 nm, (d) ICON-ART total attenuated backscatter at 532 nm for ash and sulfate, and (e) ICON-ART spherical particle fraction defined as the ratio of spherical particle mass and total aerosol mass and only areas where the ICON-ART total attenuated backscatter is larger than  $2 \times 10^{-4} \text{ km}^{-1} \text{ sr}^{-1}$  are shown. All plots correspond to 5 UTC on 13 April 2021, which is the approximate time of the CALIPSO overpass.

In large part, the volcanic plume is dominated by uncoated ash particles, as Figure 7a is dominated by values close to zero. The fraction of the spherical particle mass is on the same order or larger than the mass of uncoated particles at the plume top, the eastern edge of the plume, and directly west of the volcano close to the surface and between 10 and 15 km.

The maximum plume height assumed for emissions was 18.3 km and the vent height was about 1.2 km. However, the upper plume reached altitudes larger than 20 km. Muser et al. (2020) showed that aerosol-radiation interaction can lead to a warming of the plume and a lofting of the plume top. Lofting brought particles to regions of higher O<sub>3</sub> concentration and thus larger OH concentration, which increases aging and sulfate production. Furthermore,

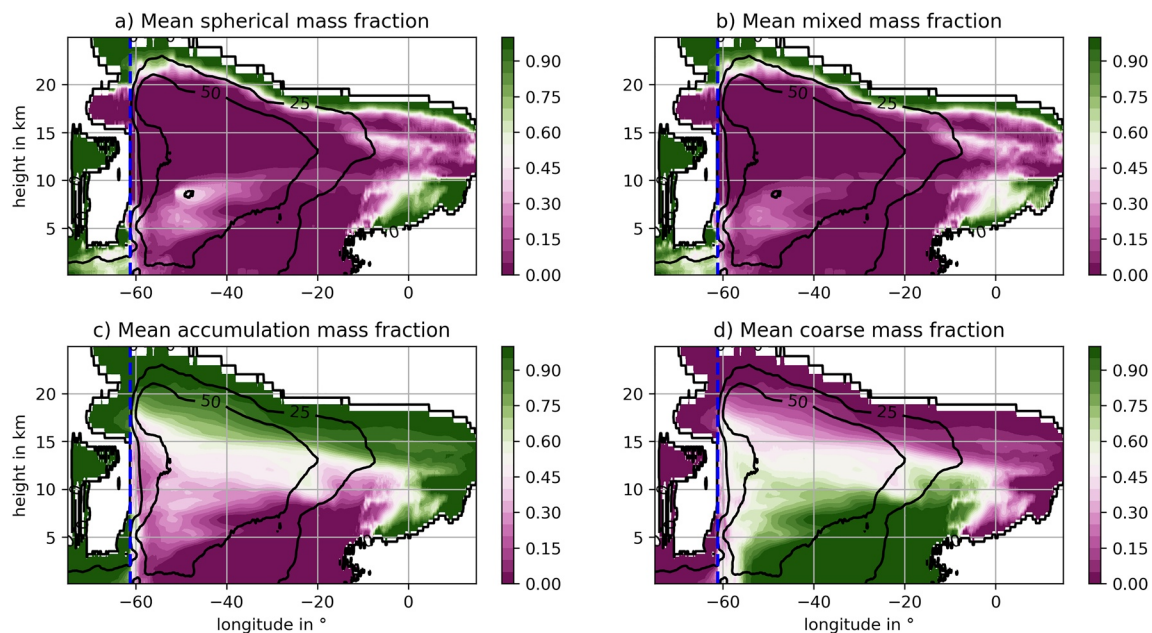


**Figure 7.** Height-longitude cross-section of temporal averages over all 96 hr for the latitudes  $\pm 2.5^\circ$  around the latitude of the volcano ( $13.33^\circ\text{N}$ ) for the (a) spherical particle mass (mixed mode + soluble mode) fraction of the total ash and sulfate mass, (b) mixed mode fraction of the total ash and sulfate mass, (c) accumulation mode fraction of the total ash mass, and the (d) coarse mode fraction of the total ash mass. The contour lines indicate the number of hours where ash is detected at the location and the blue dashed line refers to the longitude of the La Soufrière eruption.

ash aging increases the scattering properties in the SW range slightly compared to pure ash particles. However, the increase in SW radiation extinction for aged particles is larger than for pure ash particles (compare Figure 2 in Muser et al. (2020)). Thus, aerosol aging increases aerosol-radiation interaction, which might even lead to stronger lofting and the formation of a spherical particle-dominated plume top. Although, Muser et al. (2020) found a faster removal of aged particles from the atmosphere within the first 4 days due to a stronger increase in the particle diameter, we argue that the particle growth in the upper plume is too small to significantly affect the sedimentation velocities of coated particles here.

The fraction of spherical particles increases toward the eastern edge of the plume because there is more time for sulfate production and particle aging. As the main transport pathway of the plume is eastward, we argue that more time was available for sulfate production and particle aging west of the volcano as well.

Coated ash particles make the largest contribution to the spherical particle mass, whereas the contribution of sulfate is much lower in most parts of the plume (compare Figures 7a and 7b). This is partly related to the fact that the mass of mixed particles is larger than the mass of soluble particles due to the ash core. Nevertheless, an exception occurs between  $60^\circ\text{W}$  and  $40^\circ\text{W}$  up to about 9 km. In this region, the formation of sulfate is enhanced due to the large availability of OH and water in the troposphere. With increasing distance from the source, the fraction of sulfate diminishes. This is likely due to coagulation with ash particles. The coated particles increase in diameter, which leads to faster removal from the atmosphere. We can see this in Figure 7b below 10 km between  $60^\circ\text{W}$  and  $15^\circ\text{W}$  because the mixed mode fraction also decreases with increasing distance from the source, but more slowly than the fraction of the spherical modes.

The ash plume consists mainly of particles in the accumulation mode at the plume top and particles in the coarse mode closer to the surface (Figures 7c and 7d). As coarse mode particles are larger and heavier than particles in the accumulation mode, they sediment faster and increase the fraction of larger particles from plume top toward the surface. When comparing Figures 7c and 7d, the fraction values between  $55^\circ\text{W}$  and  $60^\circ\text{W}$  and from surface to 15 km are closer to 0.5 for the coarse mode fraction than for the accumulation mode fraction. At this distance from the volcano, the plume still contains a considerable amount of particles in the giant mode. Everywhere else the colors seem to be switched, meaning the ash plume only consists of particles in the accumulation and coarse modes.

The highest fraction of coated particles in the troposphere below 13 km (Figure 7b) is collocated with the highest fraction of accumulation mode particle in the troposphere (Figure 7c). This results from the larger available surface area of accumulation mode particles compared to coarse mode particles, which increases the condensation of  $\text{H}_2\text{SO}_4$  onto ash particles. Furthermore, the shift from the insoluble mode into the mixed mode occurs faster because the threshold of 5% soluble mass on insoluble ash is reached earlier.

#### 4. Discussion and Conclusion

In this paper, we performed an ICON-ART simulation including aerosol dynamic processes such as nucleation, condensation, and coagulation to investigate aerosol aging during the first 4 days after the La Soufrière eruption in April 2021. In our model setup, ash and  $\text{SO}_2$  are emitted for each individual eruption phase separately by coupling ICON-ART to the volcanic plume rise model FPlume. This setup also allows a comparison between model and observations close to the volcano, where the individual eruption phases are still separated from each other. The main direction of the volcanic ash and  $\text{SO}_2$  volcanic plume dispersion in the model is across the tropical and subtropical Atlantic Ocean, similar to the findings by Babu et al. (2022).

We compared our results with different products from remote sensing instruments, i.e., total attenuated backscatter from CALIOP onboard CALIPSO, plume heights, AOD, fraction of spherical particles, and SSA from MISR onboard Terra, and equivalent radar reflectivity from BCO. This enables us to answer the research questions raised in Section 1.

The near-source distribution of ash particles is strongly driven by the emissions, and the consideration of the individual eruption phases is important for modeling the 2021 La Soufrière eruption. Our results show that volcanic aerosol aging begins already close to the volcano. It is especially visible in the plume part south of Barbados in both the model and observations. A comparison in the northern part is only possible to a limited extent due to the complicating presence of meteorological clouds in the MISR data. Muser et al. (2020) found that aerosol dynamics have a huge impact on the lifetime and the vertical distribution of volcanic ash in the atmosphere in the first 4 days after the Raikoke 2019 eruption. However, close to the volcano, the effect of ash aging has a minor effect on the distribution of the ash plume because the time for particle growth is short (a few hours) as revealed by our results.

The rate of aging is faster in the troposphere than above the tropopause. We argue that the lower abundance of OH in the stratosphere reduces sulfate particles nucleation and the condensation of  $\text{H}_2\text{SO}_4$  onto existing particles. Furthermore, lower relative humidity in the stratosphere reduces the condensation of water onto the aerosols. As a consequence, the coagulation of ash particles with sulfate is also reduced in the stratosphere. However, spherical particles dominate the plume top across all longitudes. Muser et al. (2020) found a lofting of the volcanic plume top due to aerosol-radiation interaction. Bruckert et al. (2022) showed that warming of ash in volcanic plumes also leads to a rise of the  $\text{SO}_2$  plume top. In addition to the previous findings from Muser et al. (2020) and Bruckert et al. (2022), we argue that lofting by aerosol-radiation interaction might be stronger for coated ash than for pure ash (at least as long as particle growth is small). Together with faster  $\text{SO}_2$  oxidation rates, this leads to a formation of a plume top dominated by spherical particles.

Section 3.4 revealed large differences in the plume heights and aerosol properties in some regions of the plume between model results and MISR observations. These regions were also largely covered by clouds which hampered a comparison of model and observations. It is possible that volcanic sulfate and ash aerosols acted as cloud condensation nuclei and ice nucleating particles, respectively. This might have formed cloud droplets and ice-coated ash particles, which appear as clouds in true color images. In the model, the interaction between aerosols and clouds was not considered and is the topic of ongoing work.

Despite the efforts to precisely represent the eruption dynamics (Bruckert et al., 2022), input parameters (e.g., the start and end time of individual eruption phases, plume heights, and exit conditions) are still major sources of uncertainty in our simulations. FPlume needs input parameters for the plume height, exit temperature, exit velocity, and exit volatile fraction. Due to the lack of direct measurements for specific eruptions, we rely on the available data and estimations based on eruptions with similar conditions (tectonic setting, explosively index, and magma composition). Based on offline analysis, we estimate the uncertainties in the MER due to errors in the input parameters to be in a range of  $\pm 20\%$ , which will not significantly change our results. Furthermore, we assume that uncertainties in the input  $\text{SO}_2$  emission are of minor relevance to the outcomes of this work,



especially because Figures 7a and 7b show that the availability of water vapor and OH is the main limiting factors for particle aging and sulfate production. The optical properties of volcanic aerosols in the model are derived assuming spherical particles and an averaged size distribution, composition, and mixing state of the individual modes (Muser et al., 2020). These assumptions can lead to further uncertainties that are discussed by Muser et al. (2020).

This study provides the first direct comparison of measured and simulated aerosol aging in volcanic eruption plumes. It confirms that the aging modulates both the size and the composition of volcanic aerosols, which has major implications for the impacts of volcanism on weather and climate.

## Data Availability Statement

The output data from the ICON-ART simulations performed for this study are available at RADAR4KIT via <https://doi.org/10.35097/878> with “CC BY-NC-ND 4.0” (Bruckert, 2023). The used ICON-ART code is license protected and can be accessed by request to the corresponding author.

## Acknowledgments

This research has been funded by the Deutsche Forschungsgemeinschaft (DFG) as part of the Research Unit VolImpact (FOR2820, DFG Grant 398006378). The contributions are within the VolImpact subprojects VolPlume (JB, GAH, and AH), VolDyn (SW), and VolClim (CT). This work used resources of the Deutsches Klimarechenzentrum (DKRZ) granted by its Scientific Steering Committee (WLA) under project ID bb1093. We acknowledge James A. Limbacher for preparing and providing us the MISR RA data, and Verity J. B. Flower for running the MISR MINX plume height algorithm for this case. We thank Fabio Cramereri for the development of scientific color maps (Cramereri, 2021) to prevent visual distortion of the data and exclusion of readers with color-vision deficiencies (Cramereri et al., 2020). These colormaps were used for Figures 2, 3, 5, 6a, 6e, and 7. Open Access funding enabled and organized by Projekt DEAL.

## References

- Abdelkader, M., Stenichikov, G., Pozzer, A., Tost, H., & Lelieveld, J. (2023). The effect of ash, water vapor, and heterogeneous chemistry on the evolution of a Pinatubo-size volcanic cloud. *Atmospheric Chemistry and Physics Discussions*, 23, 471–500. <https://doi.org/10.5194/acp-23-471-2023>
- Babu, R., Nguyen, L. S. P., Sheu, G.-R., Griffith, S. M., Pani, S. K., Huang, H.-Y., & Lin, N.-H. (2022). Long-range transport of La Soufrière volcanic plume to the western North Pacific: Influence on atmospheric mercury and aerosol properties. *Atmospheric Environment*, 268, 118806. <https://doi.org/10.1016/j.atmosenv.2021.118806>
- Bechtold, P., Köhler, M., Jung, T., Doblas-Reyes, F., Leutbecher, M., Rodwell, M. J., et al. (2008). Advances in simulating atmospheric variability with the ECMWF model: From synoptic to decadal time-scales. *Quarterly Journal of the Royal Meteorological Society*, 134(634), 1337–1351. <https://doi.org/10.1002/qj.289>
- Bruckert, J. (2023). ICON-ART data: Dispersion and aging of volcanic aerosols after the La Soufrière eruption in April 2021 [Dataset]. <https://doi.org/10.35097/878>
- Bruckert, J., Hoshyaripour, G. A., Horváth, A., Muser, L. O., Prata, F. J., Hoose, C., & Vogel, B. (2022). Online treatment of eruption dynamics improves the volcanic ash and SO<sub>2</sub> dispersion forecast: Case of the 2019 Raikoke eruption. *Atmospheric Chemistry and Physics*, 22(5), 3535–3552. <https://doi.org/10.5194/acp-22-3535-2022>
- Chouza, F., Leblanc, T., Barnes, J., Brewer, M., Wang, P., & Koon, D. (2020). Long-term (1999–2019) variability of stratospheric aerosol over Mauna Loa, Hawaii, as seen by two co-located lidars and satellite measurements. *Atmospheric Chemistry and Physics*, 20(11), 6821–6839. <https://doi.org/10.5194/acp-20-6821-2020>
- Cramereri, F. (2021). Scientific colour maps version 7.0.0 (February 2021). <https://doi.org/10.5281/zenodo.4491293>
- Cramereri, F., Shephard, G. E., & Heron, P. J. (2020). The misuse of colour in science communication. *Nature Communications*, 11(5444), 5444. <https://doi.org/10.1038/s41467-020-19160-7>
- Eriksson, A. C., Wittbom, C., Roldin, P., Sporre, M., Oström, E., Nilsson, P., et al. (2017). Diesel soot aging in urban plumes within hours under cold dark and humid conditions. *Scientific Reports*, 7(1), 12364. <https://doi.org/10.1038/s41598-017-12433-0>
- Flower, V. J. B., & Kahn, R. A. (2020). The evolution of Icelandic volcano emissions, as observed from space in the Era of NASA's Earth Observing System (EOS). *Journal of Geophysical Research: Atmospheres*, 125, e2019JD031625. <https://doi.org/10.1029/2019JD031625>
- Folch, A., Costa, A., & Macedonio, G. (2016). FPLUME-1.0: An integral volcanic plume model accounting for ash aggregation. *Geoscientific Model Development*, 9(1), 431–450. <https://doi.org/10.5194/gmd-9-431-2016>
- Giorgetta, M. A., Brokopf, R., Crueger, T., Esch, M., Fiedler, S., Helmert, J., et al. (2018). ICON-A, the atmosphere component of the ICON Earth system model: I. Model description. *Journal of Advances in Modeling Earth Systems*, 10, 1613–1637. <https://doi.org/10.1029/2017MS001242>
- Gouhier, M., Eycheenne, J., Azzaoui, N., Guillin, A., Deslandes, M., Poret, M., et al. (2019). Low efficiency of large volcanic eruptions in transporting very fine ash into the atmosphere. *Scientific Reports*, 9(1), 6097. <https://doi.org/10.1038/s41598-019-42489-z>
- Heinze, R., Dipankar, A., Henken, C. C., Moseley, C., Sourdeval, O., Trömel, S., et al. (2017). Large-eddy simulations over Germany using ICON: A comprehensive evaluation. *Quarterly Journal of the Royal Meteorological Society*, 143(702), 69–100. <https://doi.org/10.1002/qj.2947>
- Horváth, A., Carr, J. L., Girina, O. A., Wu, D. L., Bril, A. A., Mazurov, A. A., et al. (2021). Geometric estimation of volcanic eruption column height from GOES-R near-limb imagery—Part 1: Methodology. *Atmospheric Chemistry and Physics*, 21(16), 12189–12206. <https://doi.org/10.5194/acp-21-12189-2021>
- Horváth, A., Carr, J. L., Wu, D. L., Bruckert, J., Hoshyaripour, G. A., & Buehler, S. A. (2022). Measurement report: Plume heights of the April 2021 La Soufrière eruptions from GOES-17 side views and GOES-16-MODIS stereo views. *Atmospheric Chemistry and Physics Discussions*, 22, 12311–12330. <https://doi.org/10.5194/acp-2022-253>
- Hoshyaripour, G. A., Bachmann, V., Förstner, J., Steiner, A., Vogel, H., Wagner, F., et al. (2019). Effects of particle nonsphericity on dust optical properties in a forecast system: Implications for model-observation comparison. *Journal of Geophysical Research: Atmospheres*, 124, 7164–7178. <https://doi.org/10.1029/2018JD030228>
- Joseph, E. P., Camejo-Harry, M., Christopher, T., Contreras-Arratia, R., Edwards, S., Graham, O., et al. (2022). Responding to eruptive transitions during the 2020–2021 eruption of La Soufrière volcano, St. Vincent. *Nature Communications*, 13(1), 4129. <https://doi.org/10.1038/s41467-022-31901-4>
- Ka-Band Cloud Radar. (2022). Ka-Band Cloud Radar. Retrieved from <https://wiki.mpimet.mpg.de/doku.php?id=observations:bco:cloudradars:coralradar>
- Kahn, R. A., Banerjee, P., & McDonald, D. (2001). Sensitivity of multiangle imaging to natural mixtures of aerosols over ocean. *Journal of Geophysical Research*, 106(D16), 18219–18238. <https://doi.org/10.1029/2000JD900497>



- Kahn, R. A., & Gaitley, B. J. (2015). An analysis of global aerosol type as retrieved by MISR. *Journal of Geophysical Research: Atmospheres*, 120, 4248–4281. <https://doi.org/10.1002/2015JD023322>
- Kahn, R. A., & Limbacher, J. (2012). Eyjafjallajökull volcano plume particle-type characterization from space-based multi-angle imaging. *Atmospheric Chemistry and Physics*, 12(20), 9459–9477. <https://doi.org/10.5194/acp-12-9459-2012>
- Klingebiel, M., Ghate, V. P., Naumann, A. K., Ditas, F., Pöhlker, M. L., Pöhlker, C., et al. (2019). Remote sensing of sea salt aerosol below trade wind clouds. *Journal of the Atmospheric Sciences*, 76(5), 1189–1202. <https://doi.org/10.1175/JAS-D-18-0139.1>
- Limbacher, J. A., & Kahn, R. A. (2014). MISR research-aerosol-algorithm refinements for dark water retrievals. *Atmospheric Measurement Techniques*, 7(11), 3989–4007. <https://doi.org/10.5194/amt-7-3989-2014>
- Malave, F. F., Haywood, J. M., Jones, A., Gettelman, A., Clarisse, L., Bauduin, S., et al. (2017). Strong constraints on aerosol-cloud interactions from volcanic eruptions. *Nature*, 546(7659), 485–491. <https://doi.org/10.1038/nature22974>
- Marshall, L. R., Maters, E. C., Schmidt, A., Timmreck, C., Robock, A., & Toohey, M. (2022). Volcanic effects on climate: Recent advances and future avenues. *Bulletin of Volcanology*, 84(5), 54. <https://doi.org/10.1007/s00445-022-01559-3>
- Marti, A., Folch, A., Jorba, O., & Janjic, Z. (2017). Volcanic ash modeling with the online NMMB-MONARCH-ASH v1.0 model: Model description, case simulation, and evaluation. *Atmospheric Chemistry and Physics*, 17(6), 4005–4030. <https://doi.org/10.5194/acp-17-4005-2017>
- Maters, E. C., Cimarelli, C., Casas, A. S., Dingwell, D. B., & Murray, B. J. (2020). Volcanic ash ice-nucleating activity can be enhanced or depressed by ash-gas interaction in the eruption plume. *Earth and Planetary Science Letters*, 551, 116587. <https://doi.org/10.1016/j.epsl.2020.116587>
- Mitra, A., Di Girolamo, L., Hong, Y., Zhan, Y., & Mueller, K. J. (2021). Assessment and error analysis of Terra-MODIS and MISR cloud-top heights through comparison with ISS-CATS Lidar. *Journal of Geophysical Research: Atmospheres*, 126, e2020JD034281. <https://doi.org/10.1029/2020JD034281>
- Morton, B. R., Taylor, G., & Turner, J. S. (1956). Turbulent gravitational convection from maintained and instantaneous sources. *Proceedings of the Royal Society of London Series A*, 234(1196), 1–23. <https://doi.org/10.1098/rspa.1956.0011>
- MPI-M. (2021). Data from the BCO during the time-period of the Soufriere eruption [Dataset]. Retrieved from <https://observations.mpimet.mpg.de/repository/entry/show?entryid=656dc652-e02f-43c9-9378-7307a5143377>
- Muser, L. O., Hoshyaripour, G. A., Bruckert, J., Horváth, A., Malinina, E., Wallis, S., et al. (2020). Particle aging and aerosol-radiation interaction affect volcanic plume dispersion: Evidence from the Raikoke 2019 eruption. *Atmospheric Chemistry and Physics*, 20(23), 15015–15036. <https://doi.org/10.5194/acp-20-15015-2020>
- Nelson, D. L., Chen, Y., Kahn, R. A., Diner, D. J., & Mazzoni, D. (2008). Example applications of the MISR Interactive eXplorer (MINX) software tool to wildfire smoke plume analyses. In W. M. Hao (Ed.), *Remote sensing of fire: Science and application* (Vol. 7089, pp. 65–75). SPIE. <https://doi.org/10.1117/12.795087>
- Nelson, D. L., Garay, M. J., Kahn, R. A., & Dunst, B. A. (2013). Stereoscopic height and wind retrievals for aerosol plumes with the MISR Interactive eXplorer (MINX). *Remote Sensing*, 5(9), 4593–4628. <https://doi.org/10.3390/rs5094593>
- Niemeier, U., Riede, F., & Timmreck, C. (2021). Simulation of ash clouds after a Laacher See-type eruption. *Climate of the Past*, 17(2), 633–652. <https://doi.org/10.5194/cp-17-633-2021>
- Niemeier, U., Timmreck, C., Graf, H.-F., Kinne, S., Rast, S., & Self, S. (2009). Initial fate of fine ash and sulfur from large volcanic eruptions. *Atmospheric Chemistry and Physics*, 9(22), 9043–9057. <https://doi.org/10.5194/acp-9-9043-2009>
- Prata, F., Woodhouse, M., Huppert, H. E., Prata, A., Thordarson, T., & Carn, S. (2017). Atmospheric processes affecting the separation of volcanic ash and SO<sub>2</sub> in volcanic eruptions: Inferences from the May 2011 Grímsvötn eruption. *Atmospheric Chemistry and Physics*, 17(17), 10709–10732. <https://doi.org/10.5194/acp-17-10709-2017>
- Rieger, D., Bangert, M., Bischoff-Gauss, I., Förstner, J., Lundgren, K., Reinert, D., et al. (2015). ICON-ART 1.0—A new online-coupled model system from the global to regional scale. *Geoscientific Model Development*, 8(6), 1659–1676. <https://doi.org/10.5194/gmd-8-1659-2015>
- Riemer, N., Vogel, H., Vogel, B., & Fiedler, F. (2003). Modeling aerosols on the mesoscale-γ: Treatment of soot aerosol and its radiative effects. *Journal of Geophysical Research*, 108(D19), 4601. <https://doi.org/10.1029/2003JD003448>
- Robock, A. (2000). Volcanic eruptions and climate. *Reviews of Geophysics*, 38(2), 191–219. <https://doi.org/10.1029/1998RG000054>
- Rose, W. I., & Durant, A. J. (2009). Fine ash content of explosive eruptions. *Journal of Volcanology and Geothermal Research*, 186(1–2), 32–39. <https://doi.org/10.1016/j.jvolgeores.2009.01.010>
- Schneider, D. J., Rose, W. I., Coke, L. R., Bluth, G. J. S., Sprod, I. E., & Krueger, A. J. (1999). Early evolution of a stratospheric volcanic eruption cloud as observed with TOMS and AVHRR. *Journal of Geophysical Research*, 104(D4), 4037–4050. <https://doi.org/10.1029/1998JD200073>
- Schröter, J., Rieger, D., Stassen, C., Vogel, H., Weimer, M., Werchner, S., et al. (2018). ICON-ART 2.1: A flexible tracer framework and its application for composition studies in numerical weather forecasting and climate simulations. *Geoscientific Model Development*, 11(10), 4043–4068. <https://doi.org/10.5194/gmd-11-4043-2018>
- Scollo, S., Kahn, R. A., Nelson, D. L., Coltelli, M., Diner, D. J., Garay, M. J., & Realmuto, V. J. (2012). MISR observations of Etna volcanic plumes. *Journal of Geophysical Research*, 117, D06210. <https://doi.org/10.1029/2011JD016625>
- Seinfeld, J. H., & Pandis, S. N. (2006). *Atmospheric chemistry and physics: From air pollution to climate change* (2nd ed.). John Wiley & Sons.
- Stenichikov, G., Ukhov, A., Osipov, S., Ahmadov, R., Grell, G., Cady-Pereira, K., et al. (2021). How does a Pinatubo-size volcanic cloud reach the middle stratosphere? *Journal of Geophysical Research: Atmospheres*, 126, e2020JD033829. <https://doi.org/10.1029/2020JD033829>
- Stevens, B., Farrell, D., Hirsch, L., Jansen, F., Nuijens, L., Serikov, I., et al. (2016). The Barbados Cloud Observatory: Anchoring investigations of clouds and circulation on the edge of the ITCZ. *Bulletin of the American Meteorological Society*, 97(5), 787–801. <https://doi.org/10.1175/BAMS-D-14-00247.1>
- Suzuki, T. (1983). A theoretical model for dispersion of Tephra. *Arc Volcanism: Physics and Tectonics*, 95–113.
- Taylor, I. A., Grainger, R. G., Prata, A. T., Proud, S. R., Mather, T. A., & Pyle, D. M. (2022). Satellite measurements of plumes from the 2021 eruption of La Soufrière, St Vincent. *Atmospheric Chemistry and Physics Discussions*, 2022, 1–33. <https://doi.org/10.5194/acp-2022-772>
- Theys, N., De Smedt, I., Yu, H., Danckaert, T., van Gent, J., Hörmann, C., et al. (2017). Sulfur dioxide retrievals from TROPOMI onboard Sentinel-5 Precursor: Algorithm theoretical basis. *Atmospheric Measurement Techniques*, 10(1), 119–153. <https://doi.org/10.5194/amt-10-119-2017>
- Theys, N., Romahn, F., & Wagner, T. (2021). S5P mission performance Centre Sulphur Dioxide Readme (s5P-MPC-BIRA-PRF-SO<sub>2</sub>, V02.04.01 ed.). Retrieved from <https://sentinel.esa.int/documents/247904/3541451/entinel-5P-Sulphur-Dioxide-Readme.pdf>
- Thomas, H. E., & Prata, A. J. (2011). Sulphur dioxide as a volcanic ash proxy during the April–May 2010 eruption of Eyjafjallajökull Volcano, Iceland. *Atmospheric Chemistry and Physics*, 11(14), 6871–6880. <https://doi.org/10.5194/acp-11-6871-2011>
- Tiedtke, M. (1989). A comprehensive mass flux scheme for cumulus parameterization in large-scale models. *Monthly Weather Review*, 117(8), 1779–1800. [https://doi.org/10.1175/1520-0493\(1989\)117<1779:ACMFSF>2.0.CO;2](https://doi.org/10.1175/1520-0493(1989)117<1779:ACMFSF>2.0.CO;2)

- Timmreck, C. (2012). Modeling the climatic effects of large explosive volcanic eruptions. *Wiley Interdisciplinary Reviews: Climate Change*, 3(6), 545–564. <https://doi.org/10.1002/wcc.192>
- Umo, N. S., Ullrich, R., Maters, E. C., Steinke, I., Benker, N., Höhler, K., et al. (2021). The influence of chemical and mineral compositions on the parameterization of immersion freezing by volcanic ash particles. *Journal of Geophysical Research: Atmospheres*, 126, e2020JD033356. <https://doi.org/10.1029/2020JD033356>
- von Savigny, C., Timmreck, C., Buehler, S. A., Burrows, J. P., Giorgetta, M., Hegerl, G., et al. (2020). The Research unit VolImpact: Revisiting the volcanic impact on atmosphere and climate—Preparations for the next big volcanic eruption. *Meteorologische Zeitschrift*, 29(1), 3–18. <https://doi.org/10.1127/metz/2019/0999>
- Weimer, M., Schröter, J., Eckstein, J., Deetz, K., Neumaier, M., Fischbeck, G., et al. (2017). An emission module for ICON-ART 2.0: Implementation and simulations of acetone. *Geoscientific Model Development*, 10(6), 2471–2494. <https://doi.org/10.5194/gmd-10-2471-2017>
- Winker, D. M., Vaughan, M. A., Omar, A., Hu, Y., Powell, K. A., Liu, Z., et al. (2009). Overview of the CALIPSO mission and CALIOP data processing algorithms. *Journal of Atmospheric and Oceanic Technology*, 26(11), 2310–2323. <https://doi.org/10.1175/2009JTECHA1281.1>
- Zängl, G., Reinert, D., Rípodas, P., & Baldauf, M. (2015). The ICON (ICOsahedral Non-hydrostatic) modelling framework of DWD and MPI-M: Description of the non-hydrostatic dynamical core. *Quarterly Journal of the Royal Meteorological Society*, 141(687), 563–579. <https://doi.org/10.1002/qj.2378>
- Zhu, Y., Toon, O. B., Jensen, E. J., Bardeen, C. G., Mills, M. J., Tolbert, M. A., et al. (2020). Persisting volcanic ash particles impact stratospheric SO<sub>2</sub> lifetime and aerosol optical properties. *Nature Communications*, 11(1), 4526. <https://doi.org/10.1038/s41467-020-18352-5>